



*Supplement of*

## **Formation drivers and photochemical effects of $\text{ClNO}_2$ in a coastal city of Southeast China**

**Gaojie Chen et al.**

*Correspondence to:* Haichao Wang (wanghch27@mail.sysu.edu.cn) and Jinsheng Chen (jschen@iue.ac.cn)

The copyright of individual parts of the supplement might differ from the article licence.

**Captions:**

**Text S1.** Detailed information of this observation site and instruments.

**Text S2.** The calibrations of  $\text{ClNO}_2$  and  $\text{N}_2\text{O}_5$  and uncertainty analysis.

**Text S3.** The model configuration of machine learning.

**Text S4.** The box model configuration.

**Text S5.** The calculations for  $\text{N}_2\text{O}_5$  uptake coefficient ( $\gamma(\text{N}_2\text{O}_5)$ ) and  $\text{ClNO}_2$  yield ( $\phi(\text{ClNO}_2)$ ).

**Text S6.** The calculations for the contribution of the heterogeneous  $\text{N}_2\text{O}_5$  uptake to daytime  $\text{ClNO}_2$  levels.

**Fig. S1** Measurement locations. (a) Location of Xiamen City in the southeast of China. (b) Location of the measurement site in Xiamen.

**Fig. S2** The dependences of  $\text{ClNO}_2$  and  $\text{N}_2\text{O}_5$  sensitivity on relative humidity.

**Fig. S3** Comparison of observed  $\text{ClNO}_2$  concentrations and simulated concentrations of  $\text{ClNO}_2$  by the XGBoost model.

**Fig. S4** The relationships between field-derived  $\gamma(\text{N}_2\text{O}_5)$  (a),  $\phi(\text{ClNO}_2)$  (b) and  $\text{NO}_3^-$  concentrations.

**Fig. S5** The relationships among  $\text{ClNO}_2$ , and  $\text{Cl}^-$  (a),  $\text{NO}_3^-$  (b),  $\text{JNO}_2$  (c),  $S_a$  (d) around noon.

**Fig. S6** The relationship between unknown daytime sources of  $\text{ClNO}_2$  and  $\text{JNO}_2$  around noon. The production rates of unknown daytime  $\text{ClNO}_2$  sources were calculated by subtracting the total loss rates from the total production rates. The negative values of the unknown source production rate likely result from the overestimated parameter values in our current parameterization scheme compared to actual atmospheric conditions.

**Fig. S7**  $\text{RO}_x$  ( $\text{OH} + \text{HO}_2 + \text{RO}_2$ ) radicals production rates induced by  $\text{ClNO}_2$  photolysis under the observation-average conditions and the high  $\text{ClNO}_2$  case.

**Fig. S8** Increased percentages of  $\text{RO}_x$  ( $\text{OH}$ ,  $\text{HO}_2$ ,  $\text{RO}_2$ ) radicals induced by  $\text{ClNO}_2$  photolysis under the observation-average and case conditions.

**Table S1.** Measurement techniques, time resolutions, and detection limit of observation instruments at our study site.

**Table S2.** The observation data used in the box model under the observation-average conditions and the high  $\text{ClNO}_2$  case (Unit: ppb).

**Table S3.** Summary of  $\text{ClNO}_2$  peak concentrations at different types of sites in China and other countries (Unit: ppb).

**Text S1.** Detailed information of this observation site and instruments.

The observation site is on the top of the teaching building (over 70 meters) of Institute of Urban Environment, Chinese Academy of Sciences in Xiamen, surrounded by school and residential buildings, Xinglin Bay, and several major transportation roads (Fig.S1). The observation site, called as the Atmospheric Observation Supersite, is equipped with complete measurement instruments to observe trace gases, aerosol compositions, and meteorological parameters. The continuous gas analyzers (Thermo Fisher Scientific, USA) were employed to measure  $O_3$  (TEI 49*i*),  $CO$  (TEI 48*i*),  $SO_2$  (TEI 43*i*), and  $NO_x$  (TEI 42*i*). VOC species were detected by a gas chromatography system equipped with a mass spectrometer and flame ionization detector (GC-MS/FID, TH-300B, Wuhan, China).  $PM_{2.5}$  mass concentrations and its inorganic compositions ( $NO_3^-$ ,  $SO_4^{2-}$ ,  $NH_4^+$ , and  $Cl^-$ ) were monitored using the tapered element oscillating microbalance (TEOM1405, Thermo Scientific Corp., MA, USA) and the Monitor for AeRosols and Gases in ambient Air (MARGA; ADI 2080, Applikon Analytical B.V., the Netherlands), respectively. The particle surface area concentrations ( $S_a$ ) were obtained from the ambient particle number size distribution detecting by the Scanning Mobility Particle Sizer (SMPS, TSI Inc.) and Aerodynamic Particle Size Spectrometer (APS). Meteorological factors, including air temperature (T), relative humidity (RH), atmospheric pressure (P), ultraviolet radiation (UV), wind speed (WS), and wind direction (WD) were measured by the weather station with a sonic anemometer (150WX, Airmar, USA). The data of boundary layer height (BLH) was gotten from the European Centre for Medium-Range Weather Forecasts (ECMWF) ERA5 hourly reanalysis dataset. Photolysis frequency (including  $J(O^1D)$ ,  $J(NO_2)$ ,  $J(HCHO)$ ,  $J(HONO)$ ,  $J(NO_3)$ , and  $J(H_2O_2)$ ) were detected by a photolysis spectrometer (PFS-100, Focused Photonics Inc., Hangzhou, China). The HCHO analyzer (FMS-100, Focused Photonics Inc., Hangzhou, China) was used to observe the concentrations of HCHO.

The concentrations of  $ClNO_2$  and  $N_2O_5$  were measured by an iodide-adduct Chemical Ionization-Atmospheric Pressure Interface-Long Time of Flight (Aerodyne Research Inc, USA and ToFwerk AG, Switzerland) mass spectrometer ( $I^-$ -ToF-CIMS). The ambient air is drawn into the sampling chamber through a perfluoroalkoxy (PFA) pipeline, approximately 2 meters in length with an inner diameter of 1/4 inch, at a flow rate of 10 standard liters per minute (SLPM). Subsamples of approximately 2 SLPM are then introduced into the CIMS setting. Within this setup, methyl iodine gas ( $CH_3I$ ) emitted from the heated  $CH_3I$  permeation tube (VICI) undergoes ionization as it passes through a soft X-ray ionization source (ToFwerk AG, P-type), carried by an ultra-high purity nitrogen gas ( $N_2$ ) flow at 99.999% purity and a rate of 2.7 SLPM. Reagent ions ( $I^-$  and  $I(H_2O)^-$ ) selectively participate in the ion-molecule reaction (IMR) chamber with the target gas, producing iodide clusters in the IMR chamber. These clusters are then quantified using the  $I^-$ -ToF-CIMS instrument. The background signals of the CIMS instrument were determined by introducing dry  $N_2$  into the inlet for a duration of 20 minutes. To prevent the buildup of particulate matter on the inlet tubing, we replaced the tubing weekly and flushed it with deionized water, followed by a 20-minute stream of  $N_2$  for drying.

105 Additionally, to reduce interference from the sampling inlet, we utilized a pump with a flow rate of 10 SLPM  
106 to draw the ambient sample.

### 107 108 **Text S2. The calibrations of ClNO<sub>2</sub> and N<sub>2</sub>O<sub>5</sub> and uncertainty analysis.**

109 In our study, the calibrations of ClNO<sub>2</sub> and N<sub>2</sub>O<sub>5</sub> were based on previous established methods (Thaler et  
110 al., 2011; Wang et al., 2016; Wang et al., 2022). A nitrogen (N<sub>2</sub>) flow at a rate of 50 mL·min<sup>-1</sup>, containing 6  
111 ppm of Cl<sub>2</sub>, was directed over a slurry composed of sodium nitrite (NaNO<sub>2</sub>) and sodium chloride (NaCl). This  
112 slurry facilitated the production of ClNO<sub>2</sub>, with NaCl added to minimize NO<sub>2</sub> formation as a secondary  
113 product. Subsequently, the resulting mixture containing ClNO<sub>2</sub> was conditioned to a specified RH and then  
114 sampled using the CIMS instrument. To quantify the concentrations of ClNO<sub>2</sub>, the mixed flow was directly  
115 fed into a cavity attenuated phase shift spectroscopy (CAPS) instrument to measure the baseline levels of NO<sub>2</sub>,  
116 subsequently, it was passed through a thermal dissociation tube heated to 380 °C, causing ClNO<sub>2</sub> to decompose  
117 into NO<sub>2</sub>, determined by the CAPS instrument. The differences in measured NO<sub>2</sub> concentrations between with  
118 and without thermal dissociation corresponded to the concentrations of ClNO<sub>2</sub>. For the calibration of N<sub>2</sub>O<sub>5</sub>,  
119 O<sub>3</sub> was generated by passing approximately 30 sccm of ultrapure zero air through a mercury lamp (UVP). O<sub>3</sub>  
120 then reacted with a 30 sccm flow rate of NO<sub>2</sub> to produce NO<sub>3</sub>, which subsequently reacted with NO<sub>2</sub> to yield  
121 a flow of N<sub>2</sub>O<sub>5</sub>. This N<sub>2</sub>O<sub>5</sub>-enriched flow was utilized to calibrate the CIMS measurements of N<sub>2</sub>O<sub>5</sub>. By  
122 adjusting the RH, a mixed flow containing stable N<sub>2</sub>O<sub>5</sub> was introduced into the CIMS instrument, allowing  
123 for the acquisition of a normalized humidity-dependent curve for N<sub>2</sub>O<sub>5</sub>. Although the absolute concentrations  
124 of the N<sub>2</sub>O<sub>5</sub> source were not directly quantified due to the absence of an N<sub>2</sub>O<sub>5</sub>-specific detector, the N<sub>2</sub>O<sub>5</sub>-  
125 enriched flow was passed through a supersaturated NaCl solution assuming 100% conversion efficiency from  
126 N<sub>2</sub>O<sub>5</sub> to ClNO<sub>2</sub>. The dependences of ClNO<sub>2</sub> and N<sub>2</sub>O<sub>5</sub> sensitivity on RH are shown in Fig. S2, indicating that  
127 the sensitivities of ClNO<sub>2</sub> and N<sub>2</sub>O<sub>5</sub> depended on the variations of RH values. The sensitivity of ClNO<sub>2</sub> and  
128 N<sub>2</sub>O<sub>5</sub> was determined to be  $0.062 \pm 0.009$  ncps·ppb<sup>-1</sup> and  $0.15 \pm 0.018$  ncps·ppb<sup>-1</sup>, with an uncertainty of ~15%  
129 for ClNO<sub>2</sub> and ~12% for N<sub>2</sub>O<sub>5</sub>, respectively. The detection limit (3σ) of ClNO<sub>2</sub> and N<sub>2</sub>O<sub>5</sub> was 1.3 and 0.61 ppt,  
130 respectively.

### 131 132 **Text S3. The model configuration of machine learning.**

133 The gradient boosted tree implemented from XGBoost was chosen as machine learning methods. It has  
134 been optimized to run in distributed computing environment and can handle a large amount of input data.  
135 Compared to neural networks, the results of gradient boosting tree models are more interpretable, enabling  
136 them to link the results with the recognizable chemical features. The XGBoost algorithm is a tree-based  
137 machine learning model known for its excellent performance in speed and accuracy. It can aggregate weak  
138 learners into a strong model, enhancing single generalization ability and robustness, thereby improving  
139 prediction accuracy.

In this study, ClNO<sub>2</sub> concentrations are as dependent variable, and trace gases (SO<sub>2</sub>, CO, NO<sub>2</sub>, NO, O<sub>3</sub>, and N<sub>2</sub>O<sub>5</sub>), PM<sub>2.5</sub>, inorganic compositions (NO<sub>3</sub><sup>-</sup>, SO<sub>4</sub><sup>2-</sup>, NH<sub>4</sub><sup>+</sup>, and Cl<sup>-</sup>), and meteorological parameters (T, RH, UV, WS, WD, and BLH) are as the argument. In the XGBoost model, 70% of the observed data are used as the training set, and the rest 30% data are used as the testing set. Five cross-validation is employed to adjust hyperparameters to stabilize the predictive ability of the model. The adjusted hyperparameters include maximum depth, learning rate, gamma, minimum child weight, and estimate. R<sup>2</sup>, mean square error (MSE), and root mean square error (RMSE) are used to assess the model performance. The Shapely additive explanations (SHAP) model is an interpreter package designed to investigate the contributions of each feature to the model predictions. Its approach involves an additive explanatory model which treats all features as contributors, a concept inspired by cooperative game theory. For each predicted sample, the SHAP model provides a Shapley value, which is the sum of the values assigned to each feature.

#### Text S4. The box model configuration and output.

The observation-based model (OBM) coupled with the Master Chemical Mechanism (MCM) version 3.3.1 was utilized to assess the impacts of ClNO<sub>2</sub> on photochemically atmospheric oxidation. As delineated in earlier studies (Xue et al., 2015; Tham et al., 2016; Xia et al., 2021; Peng et al., 2021; Peng et al., 2022), established chlorine chemistry mechanisms have been integrated. The impacts of dilution mixing were included for all species by introducing a dilution factor, defined as a function of the variation of the planetary boundary layer (PBL) height. In our study, ClNO<sub>2</sub>, N<sub>2</sub>O<sub>5</sub>, VOCs, HCHO, HONO, CO, O<sub>3</sub>, NO, NO<sub>2</sub>, SO<sub>2</sub>, along with meteorological factors as observation constrained were input into the box model at an hourly resolution. We performed the OBM for 5 days to initialize the unconstrained compounds and radicals before starting the simulation. We focused on elucidating the influence of ClNO<sub>2</sub> photolysis on the formation of RO<sub>x</sub> radicals and O<sub>3</sub>, the AOC. Generally, the reactions of HO<sub>2</sub> + NO and RO<sub>2</sub> + NO are the major O<sub>3</sub> production pathways Eq. (S1), and the O<sub>3</sub> loss pathways Eq. (S2) include NO<sub>2</sub> + OH/RO<sub>2</sub>, O<sub>3</sub> photolysis, O<sub>3</sub> + OH/HO<sub>2</sub> radicals, O<sub>3</sub>/NO<sub>3</sub>+ VOCs. The O<sub>3</sub> production rate minus the O<sub>3</sub> loss rate was used to calculate the net O<sub>3</sub> production rate Eq. (S3).

$$P(O_3) = k_1[HO_2][NO] + \sum(k_2[RO_2][NO]) \quad (S1)$$

$$L(O_3) = k_3[O_1D][H_2O] + k_4[O_3][OH] + k_5[O_3][HO_2] + k_6[NO_2][OH] + \sum(k_7[O_3][VOCs]) + 2\sum(k_8[NO_3][VOCs]) \quad (S2)$$

$$P_{net}(O_3) = P(O_3) - L(O_3) \quad (S3)$$

Where,  $k_i$  stands for the rate constant.

The AOC is calculated by the sum of the rates of CH<sub>4</sub>, CO, and VOCs oxidized by atmospheric oxidants (O<sub>3</sub>, OH, Cl, and NO<sub>3</sub> radicals) (Xue et al., 2015; Yi et al., 2023), used by Eq. (S4).

$$AOC = \sum_i k_{Y_i}[Y_i][X] \quad (S4)$$

Where,  $[Y_i]$  is the concentrations of reduced species (VOCs, CO, and CH<sub>4</sub>),  $[X]$  is the concentrations of

oxidants (O<sub>3</sub>, OH, Cl, and NO<sub>3</sub> radicals), and  $k_{Yi}$  represents the reaction rate constant of  $Y_i$  and  $X$ .

**Text S5. The calculations for N<sub>2</sub>O<sub>5</sub> uptake coefficient ( $\gamma(\text{N}_2\text{O}_5)$ ) and ClNO<sub>2</sub> yield ( $\phi(\text{ClNO}_2)$ ).**

The N<sub>2</sub>O<sub>5</sub> uptake coefficient ( $\gamma(\text{N}_2\text{O}_5)$ ) and ClNO<sub>2</sub> yield ( $\phi(\text{ClNO}_2)$ ) were estimated using the observational data and parameterization. We derived the values of  $\gamma(\text{N}_2\text{O}_5)$  and  $\phi(\text{ClNO}_2)$  based on increased rates of ClNO<sub>2</sub> and particle nitrate (NO<sub>3</sub><sup>-</sup>) in the field observation (Phillips et al., 2016). Specially,  $\gamma(\text{N}_2\text{O}_5)$  and  $\phi(\text{ClNO}_2)$  were calculated by Eq. (S5) and (S6).

$$\gamma(\text{N}_2\text{O}_5) = \frac{2 \times (P(\text{ClNO}_2) + P(\text{NO}_3^-))}{c\text{N}_2\text{O}_5 S_a [\text{N}_2\text{O}_5]} \quad (\text{S5})$$

$$\phi(\text{ClNO}_2) = 2 \times \left( 1 + \frac{P(\text{NO}_3^-)}{P(\text{ClNO}_2)} \right)^{-1} \quad (\text{S6})$$

Here,  $P(\text{ClNO}_2)$  and  $P(\text{NO}_3^-)$  represent the production rates of ClNO<sub>2</sub> and NO<sub>3</sub><sup>-</sup> induced by N<sub>2</sub>O<sub>5</sub> uptake, respectively.  $S_a$  denotes the aerosol surface area, and  $c(\text{N}_2\text{O}_5)$  is the mean molecular speed of N<sub>2</sub>O<sub>5</sub>. This method assumes that air masses remain relatively stable, and ClNO<sub>2</sub> and NO<sub>3</sub><sup>-</sup> were produced through nighttime N<sub>2</sub>O<sub>5</sub> heterogeneous uptake. More details on the method are provided elsewhere (Tham et al., 2018; Niu et al., 2022; Phillips et al., 2016). Using the method and selection criteria, we derived  $\gamma(\text{N}_2\text{O}_5)$  and  $\phi(\text{ClNO}_2)$  during the whole measurement period.

**Text S6. The calculations for the contribution of the heterogeneous N<sub>2</sub>O<sub>5</sub> uptake to daytime ClNO<sub>2</sub> levels.**

Using a box model, we quantified: (1) the contribution of heterogeneous N<sub>2</sub>O<sub>5</sub> uptake to ClNO<sub>2</sub> production (S7), and (2) ClNO<sub>2</sub> loss via photolysis, aerosol uptake, and reaction with OH· (S8-S10). By subtracting the total loss rates from the total production rates, we estimated the production rates of the unknown ClNO<sub>2</sub> sources.



Heterogeneous uptake of N<sub>2</sub>O<sub>5</sub> and ClNO<sub>2</sub> by aerosols were implemented into the box model, following the first-order loss approach:

$$\frac{d[X]}{dt} = -\frac{c\gamma}{4} S[X] \quad (\text{S11})$$

Where  $X$  represents N<sub>2</sub>O<sub>5</sub> or ClNO<sub>2</sub>,  $c$  is the mean thermal velocity of  $X$  (cm·s<sup>-1</sup>),  $S$  is the aerosol surface area concentrations (cm<sup>2</sup>·cm<sup>-3</sup>), and  $\gamma$  is the uptake coefficient. In this study, we used an uptake coefficient of N<sub>2</sub>O<sub>5</sub> ( $\gamma(\text{N}_2\text{O}_5)$ ) value of 0.06, a production efficiency of ClNO<sub>2</sub> ( $\phi(\text{ClNO}_2)$ ) value of 1.0, and an uptake coefficient of ClNO<sub>2</sub> ( $\gamma(\text{ClNO}_2)$ ) value of 0.006 in our model, which represent upper-end estimates based on field studies (Mcduffie et al., 2018a; Mcduffie et al., 2018b).

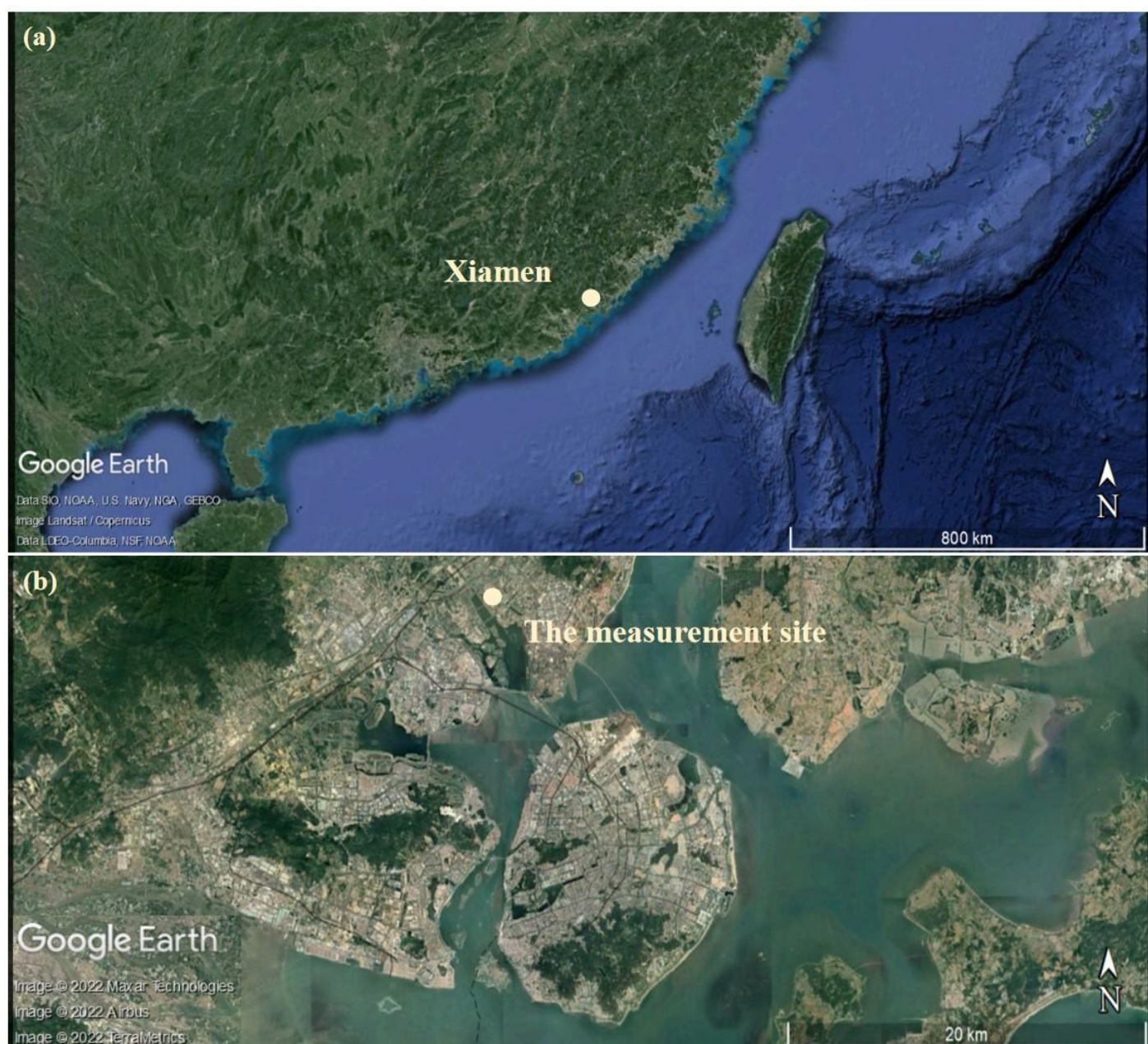


**Fig. S1** Measurement locations. (a) Xiamen City in the southeast of China. (b) Location of the measurement site in Xiamen. (The topographic image is provided by © Google Earth.)

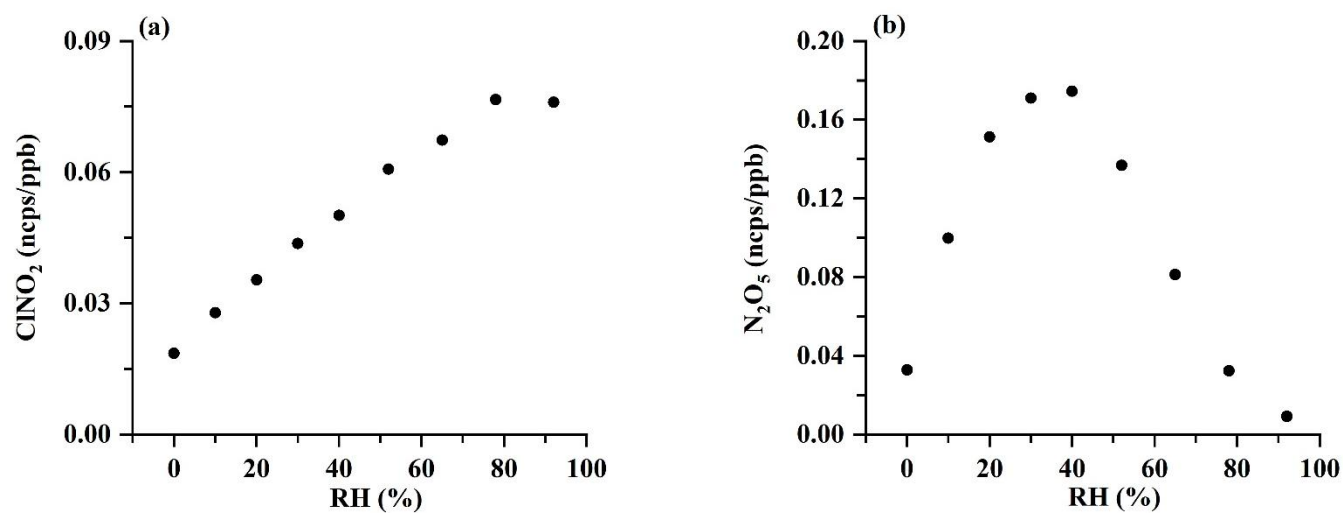


**Fig. S2** The dependences of  $\text{ClNO}_2$  and  $\text{N}_2\text{O}_5$  sensitivity on relative humidity.



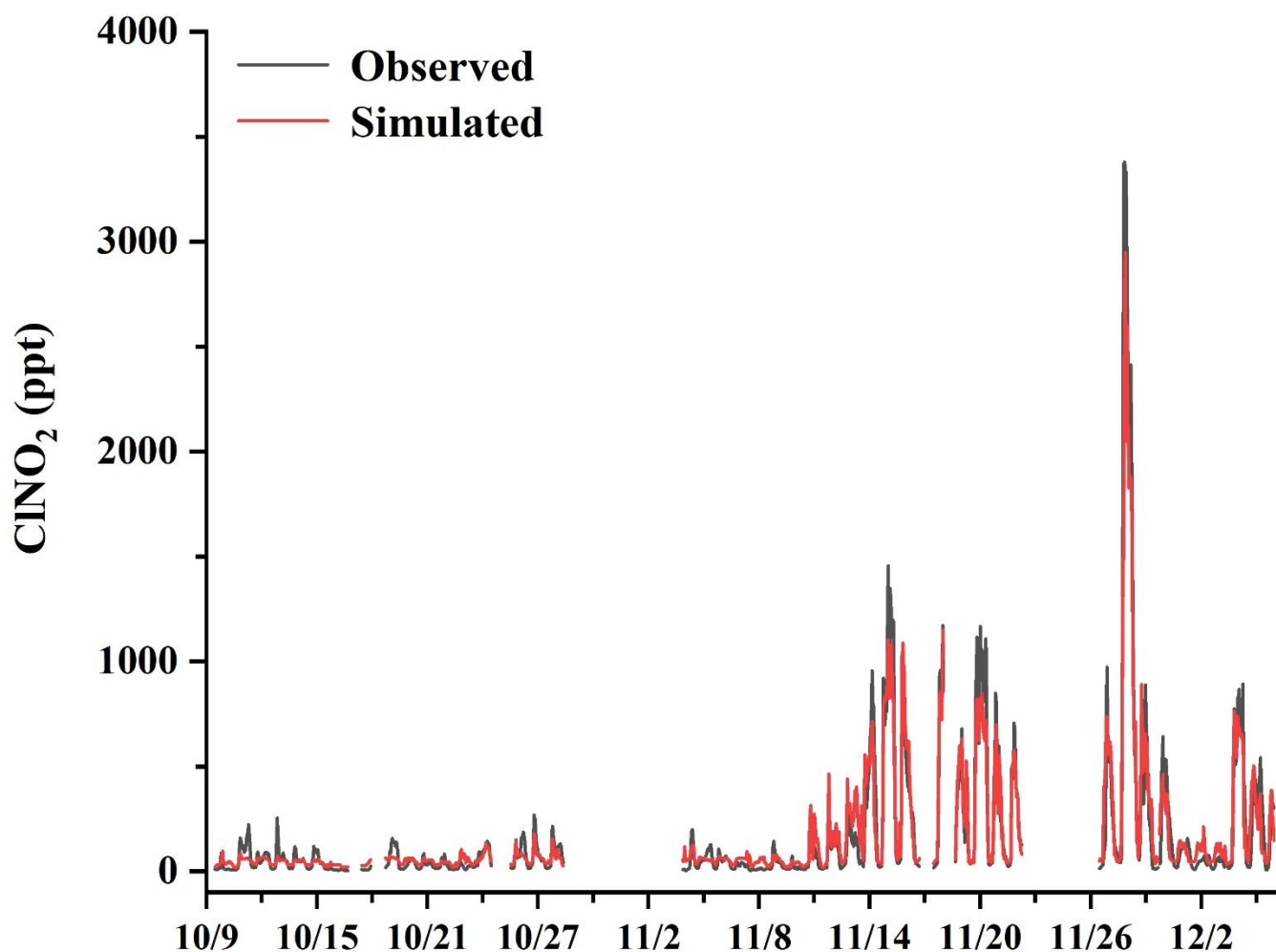


**Fig. S3** Comparison of observed  $\text{ClNO}_2$  concentrations and simulated concentrations of  $\text{ClNO}_2$  by the XGBoost model.

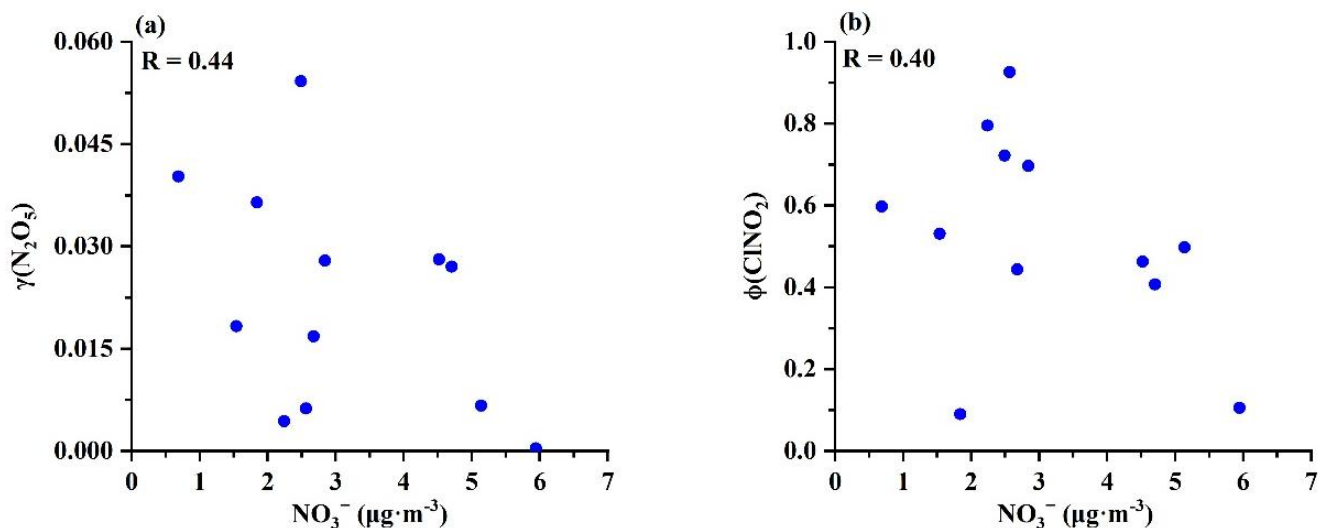


**Fig. S4** The relationships between field-derived  $\gamma(\text{N}_2\text{O}_5)$  (a),  $\phi(\text{ClNO}_2)$  (b) and  $\text{NO}_3^-$  concentrations.

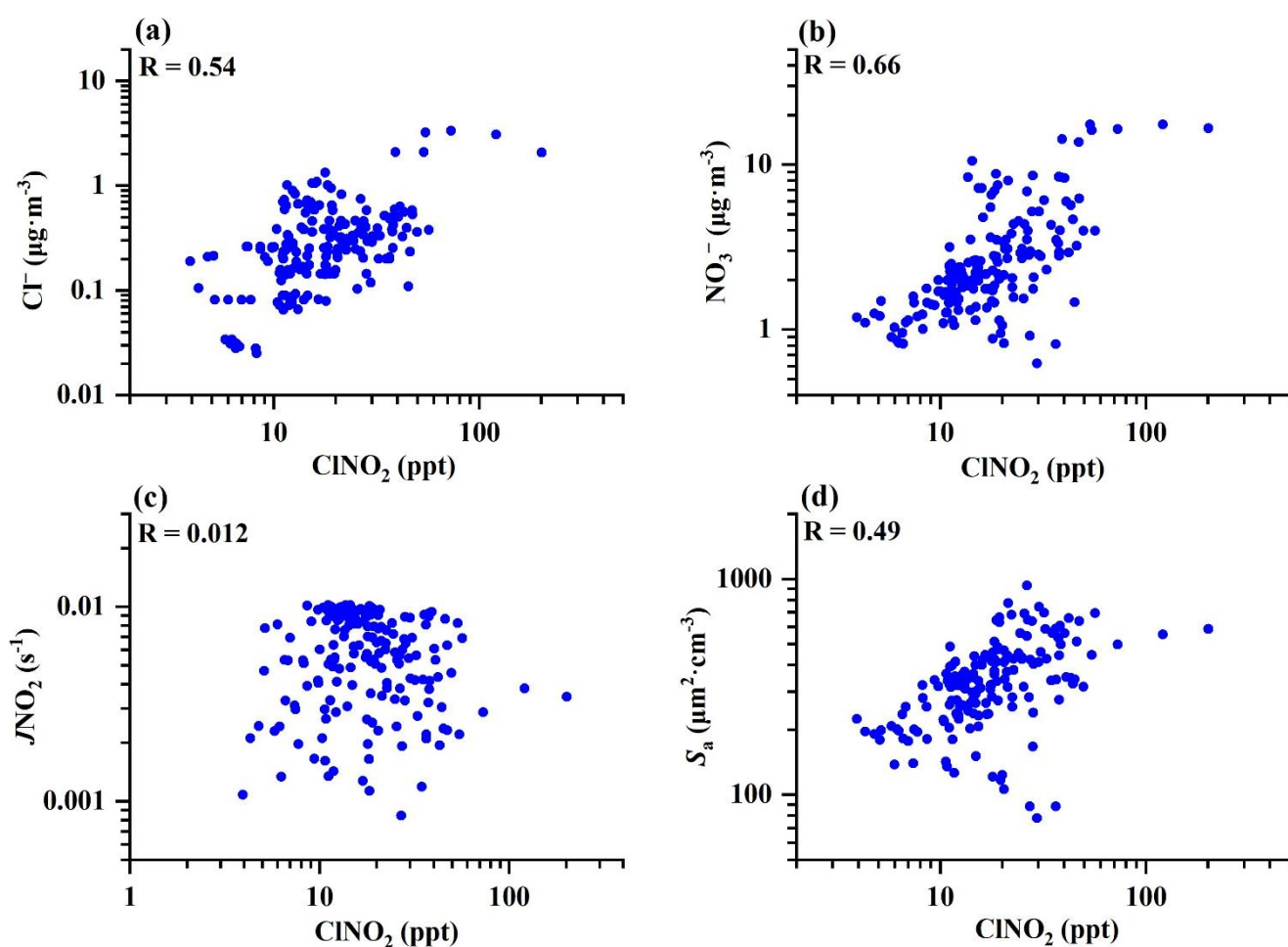


**Fig. S5** The relationships among  $\text{ClNO}_2$ , and  $\text{Cl}^-$  (a),  $\text{NO}_3^-$  (b),  $J\text{NO}_2$  (c),  $S_a$  (d) around noon.

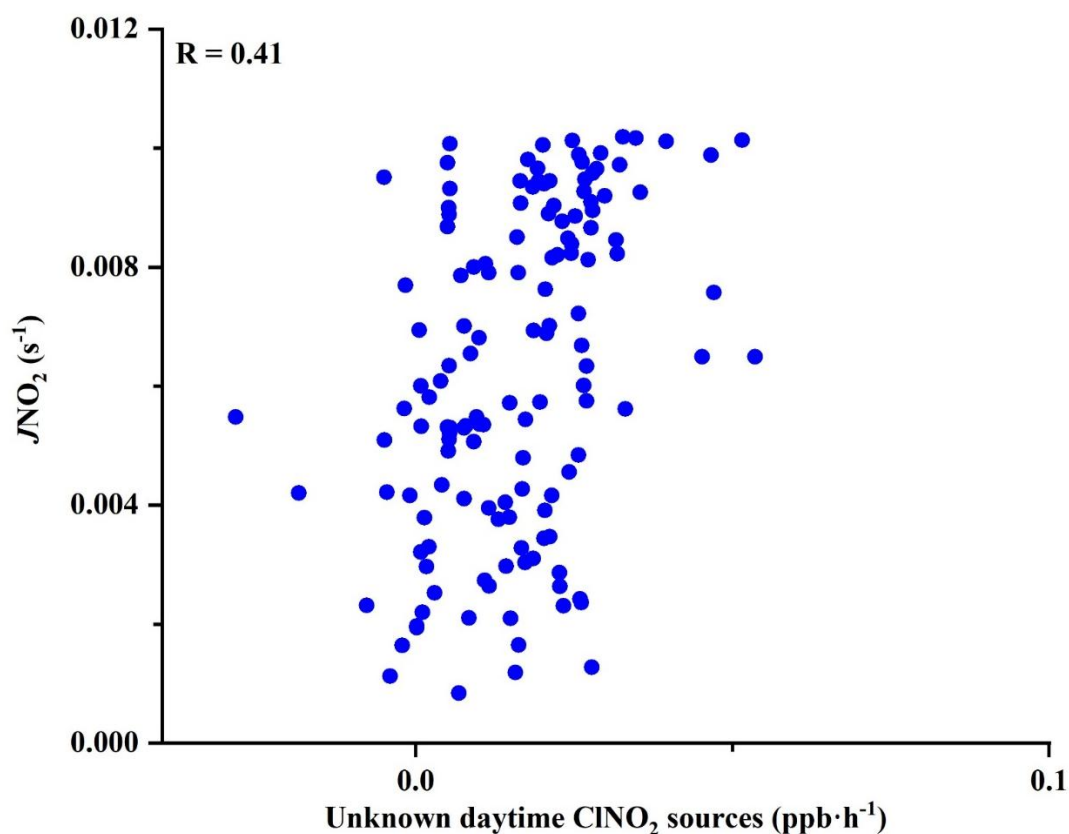


**Fig. S6** The relationship between unknown daytime sources of  $\text{ClNO}_2$  and  $\text{JNO}_2$  around noon. The production rates of unknown daytime  $\text{ClNO}_2$  sources were calculated by subtracting the total loss rates from the total production rates. The negative values of the unknown source production rate likely result from the overestimated parameter values in our current parameterization scheme compared to actual atmospheric conditions.

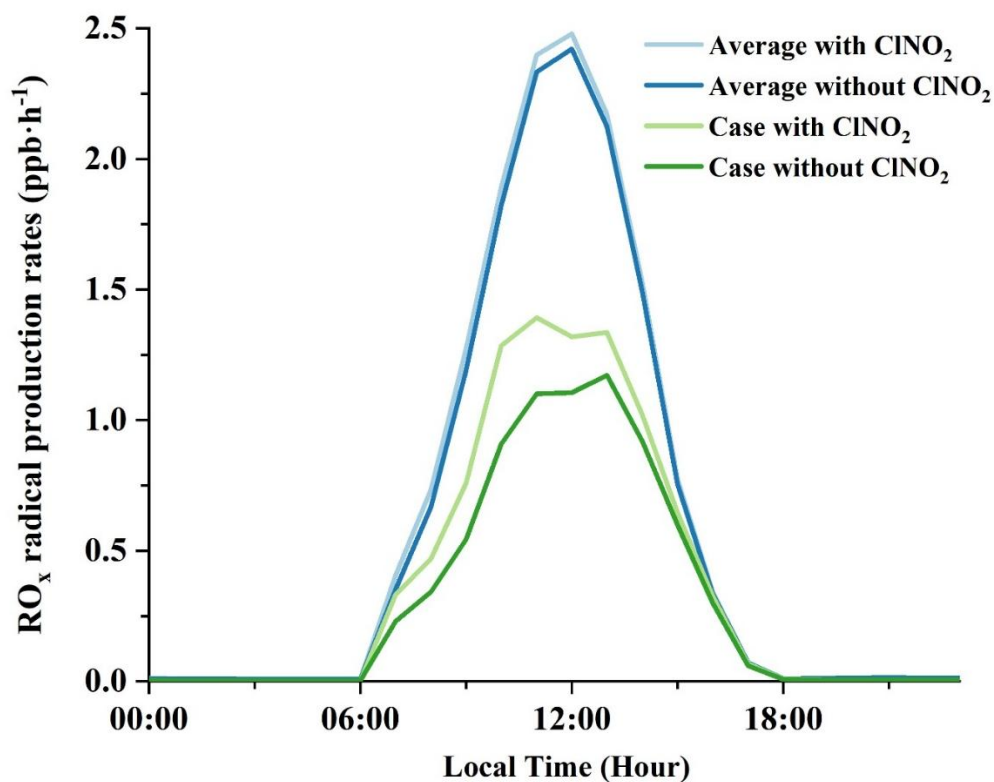


**Fig. S7** RO<sub>x</sub> (OH + HO<sub>2</sub> + RO<sub>2</sub>) radicals production rates induced by ClNO<sub>2</sub> photolysis under the observation-average conditions and the high ClNO<sub>2</sub> case.

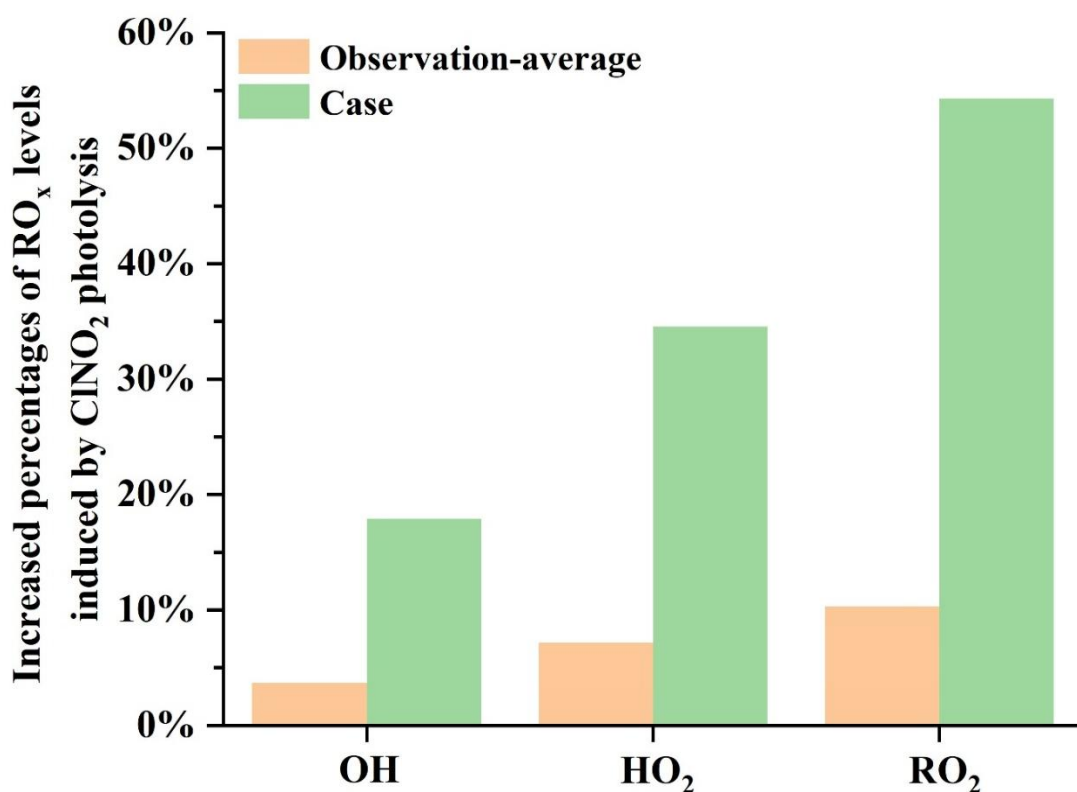


**Fig. S8** Increased percentages of RO<sub>x</sub> (OH, HO<sub>2</sub>, RO<sub>2</sub>) radicals induced by ClNO<sub>2</sub> photolysis under the observation-average conditions and the high ClNO<sub>2</sub> case.

**Table S1.** Measurement techniques, time resolutions, and detection limit of observation instruments at our study site.

Parameters	Techniques	Time resolutions	Limit of detection
ClNO <sub>2</sub> and N <sub>2</sub> O <sub>5</sub>	I <sup>-</sup> -ToF-CIMS	1 min	~ 1 ppt
CH <sub>4</sub>	NCMS6300	15 min	21 ppb
VOCs	GC-MS/FID	1 hour	0.02-0.30 ppb
HCHO	Hantzsch fluorimetry	1 s	0.05 ppb
<i>J</i> (O <sup>1</sup> D), <i>J</i> (NO <sub>2</sub> ), <i>J</i> (HONO), <i>J</i> (NO <sub>3</sub> ), <i>J</i> (HCHO), and <i>J</i> (H <sub>2</sub> O <sub>2</sub> )	Photolysis spectrometer	8 s	a
CO	Infrared absorption	1 min	40.00 ppb
SO <sub>2</sub>	Pulsed UV fluorescence	1 min	0.50 ppb
O <sub>3</sub>	UV photometry	1 min	1.00 ppb
NO	Chemiluminescence	1 min	0.50 ppb
NO <sub>2</sub>	Chemiluminescence	1 min	0.50 ppb

a. Process-specific, 5 orders of magnitude lower than maximum at noon.

298

299

300

**Table S2.** The observation data used in the box model under the observation-average conditions and the high ClNO<sub>2</sub> case (Unit: ppb).

Parameters	Average	Case	Parameters	Average	Case
T (K)	296.77	295.63	M2HEX	0.04	0.04
RH (%)	65.98	88.48	M3HEX	0.06	0.08
SO <sub>2</sub>	1.93	2.34	NC7H16	0.06	0.06
NO <sub>2</sub>	12.94	26.38	TOLUENE	1.12	1.73
NO	3.19	5.85	NC8H18	0.02	0.02
CO	461.59	769.56	PXYL	0.40	0.73
O <sub>3</sub>	31.07	11.43	EBENZ	0.19	0.42
C2H4	0.89	1.41	NC9H20	0.01	0.02
C2H2	0.78	1.53	STYRENE	0.04	0.09
C2H6	2.01	2.64	OXYL	0.11	0.20
C3H6	0.24	0.23	TM124B	0.02	0.03
C3H8	1.90	3.28	TM123B	0.01	0.01
IC4H10	0.74	1.30	NC11H24	0.01	0.01
BUT1ENE	0.05	0.06	NC12H26	0.02	0.03
NC4H10	1.07	1.97	HCHO	2.50	3.92
CBUT2ENE	0.02	0.03	ACR	0.06	0.06
TBUT2ENE	0.02	0.03	CH3COCH3	1.98	2.26
IC5H12	0.61	1.46	MEK	0.47	0.52
NC5H12	0.27	0.50	CH3CL	0.39	0.33
C5H8	0.02	0.02	C4H6	0.01	0.02
M22C4	0.02	0.02	IPROPOL	0.17	0.11
M23C4	0.05	0.06	MTBE	0.10	0.19
M2PE	0.05	0.08	ETHACET	1.26	2.14
M3PE	0.08	0.13	JNO <sub>2</sub> (s <sup>-1</sup> )	0.002106	0.000981
HEX1ENE	0.00	0.00	ClNO <sub>2</sub>	0.17	0.96
NC6H14	0.09	0.15	N <sub>2</sub> O <sub>5</sub>	0.02	0.01
BENZENE	0.18	0.32	Cl <sub>2</sub>	0.01	0.05
CHEX	0.02	0.02	HONO	0.48	0.77

301

302

303

**Table S3.** Summary of ClNO<sub>2</sub> peak concentrations at different types of sites in China and other countries (Unit: ppb).

Observation Area	Observation Sites	ClNO <sub>2</sub>	References
Wangdu, China	Rural site	~3.5	1
Beijing, China	Urban site	~3.0	2
Jinan, China	Urban site	~0.8	3
Mt. Tai, China	Mountain site	~2.0	4
Changzhou, China	Suburban site	~1.3	5
Shanghai, China	Urban site	~5.7	5
Nanjing, China	Rural site	~3.7	6
Xiamen, China	Urban site	~3.4	This study
Heshan, China	Rural site	~8.1	7
Shenzhen, China	Background site	~1.7	8
Hong Kong, China	Mountain site	~4.7	9
Seoul, Korea	Urban site	~2.5	10
Hesen, Germany	Rural site	~0.8	11
London, UK	Urban site	~0.7	12
Boulder, USA	Urban site	~1.3	13
Houston, USA	Marine boundary layer	~1.2	14
Los Angeles, USA	Marine boundary layer	~3.5	15
Calgary, Canada	Urban site	~0.3	16

The references as follows: 1 (Tham et al., 2016), 2 (Ma et al., 2023), 3 (Wang et al., 2017a), 4 (Wang et al., 2017b), 5 (Li et al., 2023), 6 (Xia et al., 2020), 7 (Yun et al., 2018), 8 (Niu et al., 2022), 9 (Wang et al., 2016), 10 (Jeong et al., 2019), 11 (Phillips et al., 2012), 12 (Bannan et al., 2015), 13 (Thornton et al., 2010), 14 (Osthoff et al., 2008), 15 (Riedel et al., 2012), 16 (Mielke et al., 2011).

## References

- Bannan, T. J., Booth, A. M., Bacak, A., Muller, J. B. A., Leather, K. E., Le Breton, M., Jones, B., Young, D., Coe, H., Allan, J., Visser, S., Slowik, J. G., Furger, M., Prévôt, A. S. H., Lee, J., Dunmore, R. E., Hopkins, J. R., Hamilton, J. F., Lewis, A. C., Whalley, L. K., Sharp, T., Stone, D., Heard, D. E., Fleming, Z. L., Leigh, R., Shallcross, D. E., and Percival, C. J.: The first UK measurements of nitryl chloride using a chemical ionization mass spectrometer in central London in the summer of 2012, and an investigation of the role of Cl atom oxidation, *J. Geophys. Res. Atmos.*, 120, 5638-5657, <https://doi.org/10.1002/2014jd022629>, 2015.
- Jeong, D., Seco, R., Gu, D., Lee, Y., Nault, B. A., Knote, C. J., McGee, T., Sullivan, J. T., Jimenez, J. L., Campuzano-Jost, P., Blake, D. R., Sanchez, D., Guenther, A. B., Tanner, D., Huey, L. G., Long, R., Anderson, B. E., Hall, S. R., Ullmann, K., Shin, H., Herndon, S. C., Lee, Y., Kim, D., Ahn, J., and Kim, S.: Integration of airborne and ground observations of nitryl chloride in the Seoul metropolitan area and the implications on regional oxidation capacity during KORUS-AQ 2016, *Atmos. Chem. Phys.*, 19, 12779-12795, <https://doi.org/10.5194/acp-19-12779-2019>, 2019.
- Li, F., Huang, D. D., Nie, W., Tham, Y. J., Lou, S., Li, Y., Tian, L., Liu, Y., Zhou, M., and Wang, H.: Observation of nitrogen oxide-influenced chlorine chemistry and source analysis of Cl<sub>2</sub> in the Yangtze River Delta, China, *Atmos. Environ.*, 306, 119829, <https://doi.org/10.1016/j.atmosenv.2023.119829>, 2023.
- Ma, W., Chen, X., Xia, M., Liu, Y., Wang, Y., Zhang, Y., Zheng, F., Zhan, J., Hua, C., and Wang, Z.: Reactive Chlorine Species Advancing the Atmospheric Oxidation Capacities of Inland Urban Environments, *Environ. Sci. Technol.*, 57, 14638-14647, <https://doi.org/10.1021/acs.est.3c05169>, 2023.
- McDuffie, E. E., Fibiger, D. L., Dubé, W. P., Lopez Hilfiker, F., Lee, B. H., Jaeglé, L., Guo, H., Weber, R. J., Reeves, J. M., Weinheimer, A. J., Schroder, J. C., Campuzano-Jost, P., Jimenez, J. L., Dibb, J. E., Veres, P., Ebben, C., Sparks, T. L., Wooldridge, P. J., Cohen, R. C., Campos, T., Hall, S. R., Ullmann, K., Roberts, J. M., Thornton, J. A., and Brown, S. S.: ClNO<sub>2</sub> Yields From Aircraft Measurements During the 2015 WINTER Campaign and Critical Evaluation of the Current Parameterization, *J. Geophys. Res. Atmos.*, 123, 12,994-913,015, <https://doi.org/10.1029/2018JD029358>, 2018a.
- McDuffie, E. E., Fibiger, D. L., Dubé, W. P., Lopez-Hilfiker, F., Lee, B. H., Thornton, J. A., Shah, V., Jaeglé, L., Guo, H., Weber, R. J., Michael Reeves, J., Weinheimer, A. J., Schroder, J. C., Campuzano-Jost, P., Jimenez, J. L., Dibb, J. E., Veres, P., Ebben, C., Sparks, T. L., Wooldridge, P. J., Cohen, R. C., Hornbrook, R. S., Apel, E. C., Campos, T., Hall, S. R., Ullmann, K., and Brown, S. S.: Heterogeneous N<sub>2</sub>O<sub>5</sub> Uptake During Winter: Aircraft Measurements During the 2015 WINTER Campaign and Critical Evaluation of Current Parameterizations, *J. Geophys. Res. Atmos.*, 123, 4345-4372, <https://doi.org/10.1002/2018JD028336>, 2018b.



352 Mielke, L. H., Furgeson, A., and Osthoff, H. D.: Observation of ClNO<sub>2</sub> in a Mid-Continental Urban  
 353 Environment, *Environ. Sci. Technol.*, 45, 8889-8896, <https://doi.org/10.1021/es201955u>, 2011.

354 Niu, Y.-B., Zhu, B., He, L.-Y., Wang, Z., Lin, X.-Y., Tang, M.-X., and Huang, X.-F.: Fast Nocturnal  
 355 Heterogeneous Chemistry in a Coastal Background Atmosphere and Its Implications for Daytime  
 356 Photochemistry, *J. Geophys. Res. Atmos.*, 127, e2022JD036716, <https://doi.org/10.1029/2022JD036716>,  
 357 2022.

358 Osthoff, H. D., Roberts, J. M., Ravishankara, A. R., Williams, E. J., Lerner, B. M., Sommariva, R., Bates, T.  
 359 S., Coffman, D., Quinn, P. K., Dibb, J. E., Stark, H., Burkholder, J. B., Talukdar, R. K., Meagher, J., Fehsenfeld,  
 360 F. C., and Brown, S. S.: High levels of nitryl chloride in the polluted subtropical marine boundary layer, *Nat.*  
 361 *Geosci.*, 1, 324-328, <https://doi.org/10.1038/ngeo177>, 2008.

362 Peng, X., Wang, T., Wang, W., Ravishankara, A., George, C., Xia, M., Cai, M., Li, Q., Salvador, C. M., and  
 363 Lau, C.: Photodissociation of particulate nitrate as a source of daytime tropospheric Cl<sub>2</sub>, *Nat. Commun.*, 13,  
 364 1-10, <https://doi.org/10.1038/s41467-022-28383-9>, 2022.

365 Peng, X., Wang, W., Xia, M., Chen, H., Ravishankara, A. R., Li, Q., Saiz-Lopez, A., Liu, P., Zhang, F., Zhang,  
 366 C., Xue, L., Wang, X., George, C., Wang, J., Mu, Y., Chen, J., and Wang, T.: An unexpected large continental  
 367 source of reactive bromine and chlorine with significant impact on wintertime air quality, *Natl. Sci. Rev.*, 8,  
 368 nwaa304, <https://doi.org/10.1093/nsr/nwaa304>, 2021.

369 Phillips, G. J., Tang, M. J., Thieser, J., Brickwedde, B., Schuster, G., Bohn, B., Lelieveld, J., and Crowley, J.  
 370 N.: Significant concentrations of nitryl chloride observed in rural continental Europe associated with the  
 371 influence of sea salt chloride and anthropogenic emissions, *Geophys. Res. Lett.*, 39, L10811,  
 372 <https://doi.org/10.1029/2012gl051912>, 2012.

373 Phillips, G. J., Thieser, J., Tang, M., Sobanski, N., Schuster, G., Fachinger, J., Drewnick, F., Borrmann, S.,  
 374 Bingemer, H., Lelieveld, J., and Crowley, J. N.: Estimating N<sub>2</sub>O<sub>5</sub> uptake coefficients using ambient  
 375 measurements of NO<sub>3</sub>, N<sub>2</sub>O<sub>5</sub>, ClNO<sub>2</sub> and particle-phase nitrate, *Atmos. Chem. Phys.*, 16, 13231-13249,  
 376 <https://doi.org/10.5194/acp-16-13231-2016>, 2016.

377 Riedel, T. P., Bertram, T. H., Crisp, T. A., Williams, E. J., Lerner, B. M., Vlasenko, A., Li, S. M., Gilman, J.,  
 378 de Gouw, J., Bon, D. M., Wagner, N. L., Brown, S. S., and Thornton, J. A.: Nitryl chloride and molecular  
 379 chlorine in the coastal marine boundary layer, *Environ. Sci. Technol.*, 46, 10463-10470,  
 380 <https://doi.org/10.1021/es204632r>, 2012.

381 Thaler, R. D., Mielke, L. H., and Osthoff, H. D.: Quantification of nitryl chloride at part per trillion mixing  
 382 ratios by thermal dissociation cavity ring-down spectroscopy, *Anal. Chem.*, 83, 2761-2766,

383 <https://doi.org/10.1021/ac200055z>, 2011.

384 Tham, Y. J., Wang, Z., Li, Q., Wang, W., Wang, X., Lu, K., Ma, N., Yan, C., Kecorius, S., Wiedensohler, A.,  
 385 Zhang, Y., and Wang, T.: Heterogeneous  $\text{N}_2\text{O}_5$  uptake coefficient and production yield of  $\text{ClNO}_2$  in polluted  
 386 northern China: roles of aerosol water content and chemical composition, *Atmos. Chem. Phys.*, 18, 13155-  
 387 13171, <https://doi.org/10.5194/acp-18-13155-2018>, 2018.

388 Tham, Y. J., Wang, Z., Li, Q., Yun, H., Wang, W., Wang, X., Xue, L., Lu, K., Ma, N., Bohn, B., Li, X., Kecorius,  
 389 S., Größ, J., Shao, M., Wiedensohler, A., Zhang, Y., and Wang, T.: Significant concentrations of nitryl chloride  
 390 sustained in the morning: investigations of the causes and impacts on ozone production in a polluted region  
 391 of northern China, *Atmos. Chem. Phys.*, 16, 14959-14977, <https://doi.org/10.5194/acp-16-14959-2016>, 2016.

392 Thornton, J. A., Kercher, J. P., Riedel, T. P., Wagner, N. L., Cozic, J., Holloway, J. S., Dubé, W. P., Wolfe, G.  
 393 M., Quinn, P. K., Middlebrook, A. M., Alexander, B., and Brown, S. S.: A large atomic chlorine source inferred  
 394 from mid-continental reactive nitrogen chemistry, *Nature.*, 464, 271-274, <https://doi.org/10.1038/nature08905>,  
 395 2010.

396 Wang, H., Yuan, B., Zheng, E., Zhang, X., Wang, J., Lu, K., Ye, C., Yang, L., Huang, S., and Hu, W.: Formation  
 397 and impacts of nitryl chloride in Pearl River Delta, *Atmos. Chem. Phys.*, 22, 14837-14858,  
 398 <https://doi.org/10.5194/acp-22-14837-2022>, 2022.

399 Wang, T., Tham, Y. J., Xue, L., Li, Q., Zha, Q., Wang, Z., Poon, S. C. N., Dubé, W. P., Blake, D. R., Louie, P.  
 400 K. K., Luk, C. W. Y., Tsui, W., and Brown, S. S.: Observations of nitryl chloride and modeling its source and  
 401 effect on ozone in the planetary boundary layer of southern China, *J. Geophys. Res. Atmos.*, 121, 2476-2489,  
 402 <https://doi.org/10.1002/2015JD024556>, 2016.

403 Wang, X., Wang, H., Xue, L., Wang, T., Wang, L., Gu, R., Wang, W., Tham, Y. J., Wang, Z., and Yang, L. J.  
 404 A. e.: Observations of  $\text{N}_2\text{O}_5$  and  $\text{ClNO}_2$  at a polluted urban surface site in North China: High  $\text{N}_2\text{O}_5$  uptake  
 405 coefficients and low  $\text{ClNO}_2$  product yields, *Atmos. Environ.*, 156, 125-134,  
 406 <http://dx.doi.org/10.1016/j.atmosenv.2017.02.035>, 2017a.

407 Wang, Z., Wang, W., Tham, Y. J., Li, Q., Wang, H., Wen, L., Wang, X., and Wang, T.: Fast heterogeneous  $\text{N}_2\text{O}_5$   
 408 uptake and  $\text{ClNO}_2$  production in power plant and industrial plumes observed in the nocturnal residual layer  
 409 over the North China Plain, *Atmos. Chem. Phys.*, 17, 12361-12378, [https://doi.org/10.5194/acp-17-12361-](https://doi.org/10.5194/acp-17-12361-2017)  
 410 [2017](https://doi.org/10.5194/acp-17-12361-2017), 2017b.

411 Xia, M., Peng, X., Wang, W., Yu, C., Wang, Z., Tham, Y. J., Chen, J., Chen, H., Mu, Y., and Zhang, C.: Winter  
 412  $\text{ClNO}_2$  formation in the region of fresh anthropogenic emissions: seasonal variability and insights into daytime

413 peaks in northern China, Atmos. Chem. Phys., 21, 15985-16000, <https://doi.org/10.5194/acp-21-15985-2021>,  
414 2021.

415 Xia, M., Peng, X., Wang, W., Yu, C., Sun, P., Li, Y., Liu, Y. A. H. C. t. A.-P. O. A. C., Xu, Z., Wang, Z., Xu,  
416 Z., Nie, W., Ding, A., and Wang, T.: Significant production of ClNO<sub>2</sub> and possible source of Cl<sub>2</sub> from N<sub>2</sub>O<sub>5</sub>  
417 uptake at a suburban site in eastern China, Atmos. Chem. Phys., 20, 6147-6158, [https://doi.org/10.5194/acp-](https://doi.org/10.5194/acp-20-6147-2020)  
418 [20-6147-2020](https://doi.org/10.5194/acp-20-6147-2020), 2020.

419 Xue, L. K., Saunders, S. M., Wang, T., Gao, R., Wang, X. F., Zhang, Q. Z., and Wang, W. X.: Development of  
420 a chlorine chemistry module for the Master Chemical Mechanism, Geosci. Model Dev., 8, 3151-3162,  
421 <https://doi.org/10.5194/gmd-8-3151-2015>, 2015.

422 Yi, X., Sarwar, G., Bian, J., Huang, L., Li, Q., Jiang, S., Liu, H., Wang, Y., Chen, H., and Wang, T.: Significant  
423 Impact of Reactive Chlorine on Complex Air Pollution Over the Yangtze River Delta Region, China, J.  
424 Geophys. Res. Atmos., 128, e2023JD038898, <https://doi.org/10.1029/2023JD038898>, 2023.

425 Yun, H., Wang, T., Wang, W., Tham, Y. J., Li, Q., Wang, Z., and Poon, S. C. N.: Nighttime NO<sub>x</sub> loss and ClNO<sub>2</sub>  
426 formation in the residual layer of a polluted region: Insights from field measurements and an iterative box  
427 model, Sci. Total Environ., 622-623, 727-734, <https://doi.org/10.1016/j.scitotenv.2017.11.352>, 2018.

428